基于反谐振空芯光纤的中红外 TDLAS 系统设计及应用实验研究

孙亚丽[1,2]，朱昕玥[1]，吴达坤[1,3]，伍成[1,4]，于飞[1,3*]，李仁杰[5,6]，林鑫[5**]，赵文凯[7]

[1]中国科学院上海光学精密机械研究所高功率激光单元技术实验室，上海 201800；
[2]中国科学院大学材料科学与光电工程中心，北京 100049；
[3]国科大杭州高等研究院物理与光电工程学院，浙江 杭州 310024；
[4]中国科学技术大学物理学院，安徽 合肥 230026；
[5]中国科学院力学研究所高温气体动力学国家重点实验室，北京 100190；
[6]中国科学院大学工程学院，北京 100049；
[7]中国科学院上海光学精密机械研究所红外光学材料研究中心，上海 201800

摘要 针对燃烧诊断在 2~3 μm 波长的光谱测量需求，设计并搭建了基于反谐振空芯光纤的可调谐半导体吸收光谱（TDLAS）测量装置，开展了高温水汽在 2.5 μm 波长吸收光谱的定标与测量研究。在 2~5 μm 中红外波段，反谐振空芯光纤可实现低损、单模长距离传输，能够有效解决商用氟化物光纤多模干涉造成的 TDLAS 测量精度下降的问题。经所提 TDLAS 系统准直后光束的直径低至 2.5 mm，发散角为 0.004 rad，系统信噪比为 31 dB，相比基于氟化物光纤的 TDLAS 系统，所提系统的性能得到了极大提升。进一步分析了反谐振空芯光纤中痕量水蒸气对于 4029.52 cm^{-1} 谱线测量的影响，并通过抽真空的方式降低其影响，从而提高了系统的测量精度。

关键词 光纤；反谐振空芯光纤；激光吸收光谱；多模干涉；单模；燃烧诊断

中图分类号 O433　　**文献标志码** A　　　　　　　　　　**DOI:** 10.3788/AOS230483

1 引　　言

可调谐二极管激光吸收光谱是一种灵敏、非接触、结构简单的气体测量技术[1]，被广泛应用于高温高压环境下的气体诊断，在喷气发动机燃烧室羽流[2]、航空发动机进气道[3]、超燃冲压发动机隔离段/燃烧室[4]和气体发生器[5]等设备的流场测量中发挥着重要作用[6-7]。对于这一类复杂的实验系统，激光能量的远距离传输是实现测量的重要环节，但是自由空间光路存在以下缺点：1）激光在自由空间中的直线传输方案，在复杂环境中的适应性差；2）自由空间中，长距离光路暴露于环境中，复杂的环境因素（气体吸收、散射等）可能产生干扰；3）空间光路出射光斑随衍射效应的增强而扩大，造成信号接收系统设计复杂度增加、接收效率下降。因此，在复杂、恶劣环境中使用可调谐半导体吸收光谱（TDLAS）技术时，为了保护精密激光光源、信号处理系统，以及保持稳定的光路传输，一般使用光纤完成激光光束的远距离传输，实现气体吸收光谱在远端的实时测量。

H_2O、CO_2 和 CO 等燃烧流场产物的强吸收峰大量分布在中红外波段，故中红外波段的 TDLAS 技术在流场探测应用中发挥着重要作用。H_2O 作为燃烧的主要产物，其转振谱带的基频位于中红外光谱区，因此其中红外区域的吸收线强度远强于近红外区域，选取此波段的吸收线能够使探测极限更低、灵敏度更高，非常适用于小型设备。H_2O 位于 2.5 μm 附近的吸收线因具有以下优点，成为燃烧诊断研究中的重要工具[8-9]：1）吸收线强度高，满足在小型设备及强辐射影响下进行正常探测的要求；2）谱线干扰小，2.5 μm 处 CO_2 和 CO 的吸收线强较小，有助于提高系统的信噪比、测量精确度；3）温度敏感度高，线强度随温度变化剧烈，谱线具有较大的能级差，能确保测量精度等。在 2 μm 及以上的中红外波段，石英玻璃的声子吸收导致传统单模光纤的材料损耗迅速增加，无法适用于长距离激光

传输的应用场景。然而，以 ZBLAN 为代表的氟化物玻璃光纤和以 As_2S_3 为代表的硫系玻璃光纤所具有的声子能量比石英光纤小得多，在中红外波段具有较低的传输损耗和较宽的传输带，因此在中红外 TDLAS 检测中占据重要地位。

2015 年斯坦福大学的 Goldenstein 等[10]使用氟化物光纤，通过对乙烯燃料脉冲爆震燃烧室中的 $2.482~\mu m$ 和 $4.854~\mu m$ 波段吸收光谱的测量，实现对 H_2O 和 CO 的检测，准确度达到 3%～5%。2021 年 Cassady 等[11]通过将 4 台不同波长激光器的出射光束耦合到多模硫化物（As_2S_3）光纤，测量了 2.551、2.482、4.175、4.854 μm 4 个波长，实现了 H_2O、CO_2 和 CO 的同时探测。2022 年 Clees 等[12]提出一种新型中红外激光吸收传感器，用于测量 $3.35~\mu m$ 处生物燃料混合物（E85）的蒸气，系统中使用多模 ZBLAN 光纤输出光斑。然而，氟化物和硫系玻璃光纤普遍存在热稳定性差、化学性质不稳定、易潮解和制备难度大等问题[13]。实际使用中，商用氟化物和硫系光纤主要为多模光纤，当其作为传输介质应用到 TDLAS 系统中，不可避免地出现模间干涉现象，从而对气体吸收测量精度产生影响；同时多模光纤输出的激光光束质量差、出射光斑发散角大、空间能量分布不均。这些缺陷导致了 TDLAS 系统中激光功率利用率低、信噪比差，阻碍了 TDLAS 系统的实用化部署。

除氟化物、硫系玻璃光纤等实芯光纤外，毛细管光波导是早期发展起来的可用于中、远红外波长传输的空芯波导，因具有高功率阈值、低非线性和无端反射等优点，成为高温流场探测的有力工具[14]。2011 年 Opto-Knowledge（OKSI）公司的 Kriesel 等[15]对用于 3～14 μm 的中红外波段空芯光波导进行开发和测试，测试结果显示其传输损耗约为 1 dB/m，弯曲半径为 25 cm。2016 年斯坦福大学的 Peng 等[16]将 4 段传输不同波长激光的光纤耦合到内壁镀银的多模空芯光波导中，实现了在中红外波段对 H_2O、CO_2 和 CO 3 种组分浓度、温度等参数的同时测量。然而，这类空芯光波导的损耗较高，不适用于长距离传输，空芯内径大且不易弯折、弯曲半径大，不利于系统集成化、小型化。

反谐振空芯光纤（AR-HCF）是近年来出现的新型微结构空芯光纤，具有低损耗、宽导光通带、准单模传输的优势，已在大功率激光传能、气体激光技术光纤化等领域得到广泛应用[17-20]，是适用于中红外波段低损单模传输的新型传输媒介。反谐振空芯光纤中利用反谐振微结构包层将 99.99% 以上的光能量束缚在空气芯中，使得材料吸收等本征性质对光纤模式特性的影响显著降低[21-22]。目前，石英基反谐振空芯光纤在 2～5 μm 波段的传输损耗可以低至 0.06 dB/m@2.6 μm、0.018 dB/m@3.16 μm 和 0.24 dB/m@4.55 μm[23-24]，且实现准单模传输，低于商用多模氟化物报道的最低损耗 0.08 dB/m@2.5 μm、0.17 dB/m@4.6 μm 和 0.08 dB/m@3.6 μm（Thorlabs，双包层氟化物光纤、中红外多模氟化物光纤），展现了其在中红外波段传输中的巨大应用潜力。此外，得益于石英材料的先天优势[15,25]，中红外石英基反谐振空芯光纤具有优异的机械强度、物理和化学稳定性，同时具备良好的环境适应性。

本文针对 2.5 μm 波段 TDLAS 的应用需求，首先设计、制备了低损反谐振空芯光纤，并搭建了基于光纤传输的 TDLAS 系统；然后，比较、分析了使用自研反谐振空芯光纤和商用 ZBLAN 光纤下 TDLAS 系统在输出光斑质量、信噪比等方面的差异；最后，针对反谐振空芯光纤纤芯中的痕量水汽对于 4029.52 cm^{-1} 谱线测量的影响开展实验研究和分析。所提出的基于反谐振空芯光纤的 TDLAS 系统具有传输损耗低、传输距离长、激光光束质量高、信噪比高等优点，显示了反谐振空芯光纤在中红外波段吸收光谱检测、流场探测方面具有极大的应用潜力。

2 反谐振空芯光纤设计与制备

2.1 反谐振空芯光纤导光机理简述

反谐振空芯光纤的导光机理可通过反谐振式平面波导（ARROW）理论进行定性描述[26]，即认为反谐振空芯光纤中波长量级厚度的包层薄壁能够形成稳定的多光束干涉，从而产生类似于法布里-珀罗（F-P）腔的宽谱反射效应，如图 1 所示。

可将高折射率薄壁看作一个典型的 F-P 腔，当光束掠入射时，谐振条件为

$$k_t d = m\pi, \tag{1}$$

式中：m 为正整数；d 为石英壁厚；$k_t = \frac{2\pi}{\lambda}\sqrt{n_2^2 - n_1^2}$ 为横向波数，其中 n_1 为空气折射率；n_2 为石英折射率，λ 为入射光波长。谐振波长可表示为

$$\lambda_r = \frac{2d}{m}\sqrt{n_2^2 - n_1^2}。 \tag{2}$$

如图 1 所示：当反谐振空芯光纤中传输的光波长为谐振波长时，纤芯的能量逐渐耦合到薄壁中，并透过包层泄漏到外界，造成较高的损耗；当光波长处于反谐振状态时，薄壁的多光束干涉将大部分能量反射回纤芯，由泄漏引发的损耗迅速降低。

2.2 光纤制备、测试和仿真

实验中使用的反谐振空芯光纤是由高纯度的熔融石英玻璃管（Heraeus，F300）通过堆叠-拉制法制备而成的。图 2(a)～(d)所示为拉制反谐振空芯光纤的具体流程：首先，将石英玻璃管拉制成细长的毛细玻璃管，并将毛细玻璃管堆叠成预设的结构，其中使用短石英管在首尾两端进行结构支撑；然后，将堆叠体拉制成预制棒，再将预制棒拉制成光纤。光纤拉制过程中通过控制包层孔区域和纤芯区域的压强差来实现纤芯周围包层玻璃壁的负曲率成型。
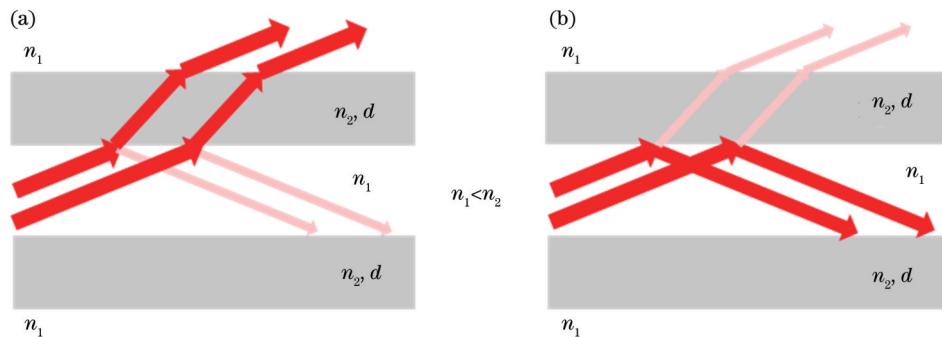
图 1　反谐振波导原理图。(a)λ满足谐振波长时光场的传输情况;(b)λ不满足谐振波长时光场的传输情况
Fig. 1　Anti-resonant waveguide schematic. (a) Transmission of the light field when the resonant wavelength is satisfied; (b) transmission of the light field when the resonant wavelength is not satisfied
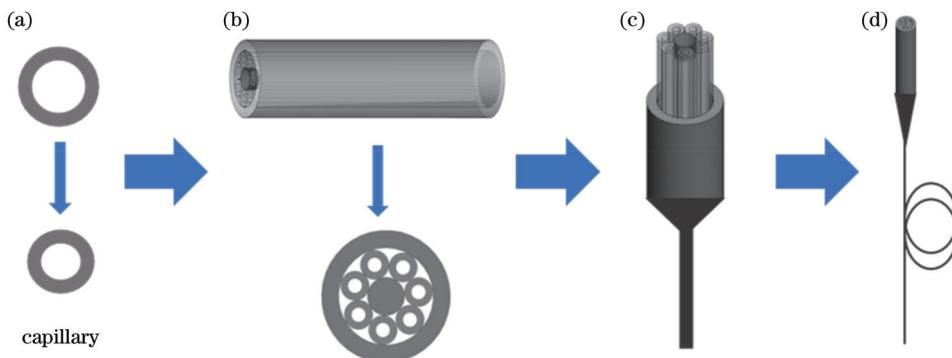

图 2　反谐振空芯光纤拉制流程。(a)拉制玻璃毛细管;(b)堆叠毛细管;(c)拉制光纤预制棒;(d)拉制光纤
Fig. 2　AR-HCF drawing flow chart. (a) Drawing glass capillary; (b) stacking capillary; (c) drawing optical fiber preform; (d) drawing optical fiber

图 3(a)所示为制备的反谐振空芯光纤端面,光纤包层中共有 7 根冰淇淋型玻璃毛细管,包层石英壁厚均匀,壁厚约为 2.1 μm,由包层冰淇淋型玻璃管围成的纤芯直径约为 43 μm,光纤外径约为 220 μm。制备的光纤总长度为 68 m,通过标准截断法(将 68 m 截断至 10 m)得到的光纤损耗结果如图 3(b)所示,可知该光纤的低损工作波长范围为 2.40~2.55 μm,其中 2.5 μm 波长处的损耗为 0.06 dB/m。
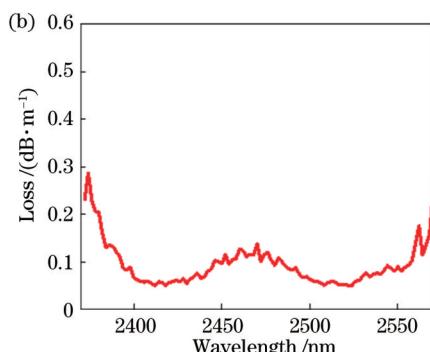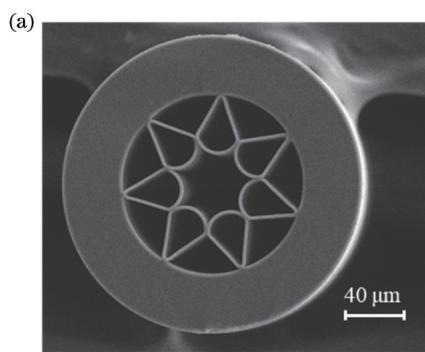
图 3　反谐振空芯光纤参数。(a)光纤端面的扫描电子显微图(光纤外径为 220 μm,纤芯直径为 43 μm);(b)光纤损耗谱
(0.06 dB/m@2.5 μm)
Fig. 3　AR-HCF parameters. (a) Scanning electron microscopy image of fiber cross section (outer diameter of the fiber is 220 μm and core diameter is 43 μm); (b) fiber loss spectrum (0.06 dB/m@2.5 μm)

为进一步研究此光纤的传输特性,参照图 3(a)建立了冰淇淋型反谐振空芯光纤的仿真模型,并利用商用有限元仿真软件 COMSOL 进行计算。计算模型中,空芯光纤芯径设为 45 μm,包层由 7 根冰淇淋型毛细管组成,其中毛细管壁厚为 2.1 μm,圆弧孔径为光纤芯径的 66%,即 29.7 μm。在模型的最外围加入完美匹配层以实现对泄漏能量的完全吸收,防止回波干扰。计算结果如图 4 所示,其中图 4(a)给出了波长为 2.5 μm 时

反谐振空芯光纤中基模(HE_{11})和二阶矢量模(TE_{01})的分布情况,图 4(b)所示为计算得到的基模和二阶矢量模的损耗。可以看到:此光纤基模被很好地限制在空芯中,低损传输带为 2.4~2.6 μm 波段,且 2.5 μm 处损耗约为 0.052 dB/m,与实测结果相近;参考实际光纤的

结构比例进行设计,使得纤芯中的二阶模与包层孔中的模式发生强烈耦合,进而造成能量外泄,并产生了极高的损耗,从而提升了光纤单模性。由此可见,所制备的冰淇淋型反谐振空芯光纤具备低损耗和单模传输的能力,可为之后的气体传感应用提供参考。
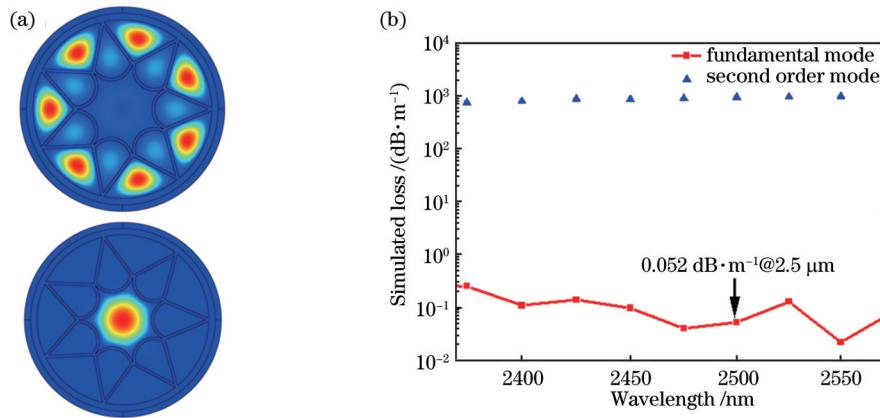

图 4　冰淇淋型反谐振空芯光纤的模场特性和传输特性仿真结果。(a)光纤中传输波长为 2.5 μm 时的 HE_{11} 模和二阶模;(b)基模和二阶模的损耗

Fig. 4　Simulation results of mode field characteristics and transmission characteristics of ice cream type AR-HCF. (a) HE_{11} mode and second order mode with a transmission wavelength of 2.5 μm in the fiber; (b) loss of the fundamental mode and second order mode

3　基于光纤的 TDLAS 实验装置

3.1　TDLAS 技术原理

TDLAS 技术以吸收光谱理论为基础,利用激光能量被待测气体分子"选频"吸收的原理来实现气体组分相关参数的测量。如图 5 所示,激光器出射激光的强度为 $I_0(\nu)$,激光通过待测气体后由光电探测器接收,透射光强为 $I(\nu)$,满足 Beer-Lambert 定律,即

$$\frac{I(\nu)}{I_0(\nu)} = \exp(-k_\nu \cdot L), \quad (3)$$

$$k_\nu = P \cdot X \cdot S(T) \cdot \phi(\nu), \quad (4)$$

$$A = k_\nu \cdot L, \quad (5)$$

$$X = \frac{A}{P \cdot S(T) \cdot L}, \quad (6)$$

式中:k_ν 为吸收系数;A 为积分吸收率;L 为吸收长度;P 为气体总压强;X 为吸收组分的物质的量浓度;$S(T)$ 为气体在温度 T 下的吸收线强度;$\phi(\nu)$ 为线型函数 $\left(\int \phi(\nu)\mathrm{d}\nu \equiv 1\right)$,在燃烧场条件下通常采用 Lorentz 线型和 Gauss 线型的卷积 Voigt 线型[27]。TDLAS 技术根据施加在激光器的扫描信号的不同可以划分为直接吸收(DAS)和波长调制(WMS)两种方案。直接吸收技术获得的是气体的绝对吸收信息,无需标定,结构简单,易于实现。但是在直接吸收法中,基线的选择会影响光谱吸收率在全波数域的积分值,因此基线的拟合对计算浓度的准确程度具有重要影响。
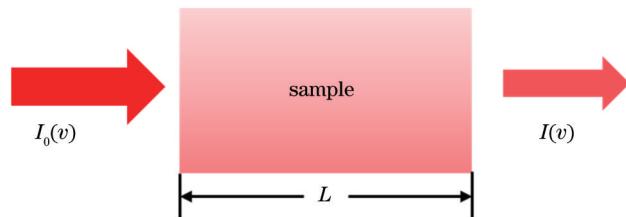
图 5　吸收光谱原理图

Fig. 5　Principle of absorption spectrum

3.2　2.5 μm 波段水蒸气的吸收光谱

在对高温火焰的直接吸收测量中,光谱信号会受到燃烧粒子和热辐射的影响,从而降低信噪比和测量精度,这就要求目标信号必须选取吸收较强的谱线来保证测量的正常进行。图 6 所示为在 2000 K 左右的温度下 H_2O 和 CO_2 在中红外波段的光谱宽带模拟结果。可以看到,H_2O 在 2.35~2.85 μm 波段的吸收较强,CO_2 在 2.6~2.85 μm 范围也存在强吸收线,容易对水蒸气吸收的测量造成干扰,因此选择干扰谱线较少的 2.5 μm 附近的 H_2O 吸收线较为合适。此波段因具有吸收强度大、干扰谱线少、温度灵敏度高等优点,在多项燃烧诊断研究中被用作探针进行流场温度、浓度、流速等重要参数的测量。

3.3　TDLAS 实验系统的搭建

图 7 所示为搭建的基于光纤的 TDLAS 系统,在(Ⅰ)中通过拆换光纤,可以较为便捷地实现反谐振空芯光纤与氟化物光纤的更换。实验中使用的多模 ZBLAN 光纤是由 ZrF_4、BaF_2、LaF_3、AlF_3、NaF 和 HfF_4
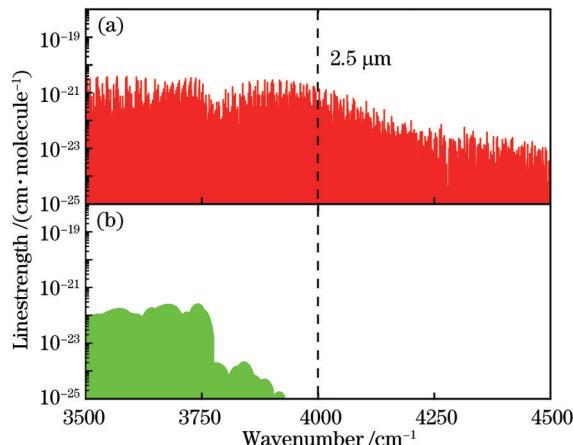
图 6 2000 K 时 H_2O、CO_2 的近红外和中红外波段的线强(数据来自 HITRAN2016)。(a) H_2O;(b) CO_2

Fig. 6 Near-infrared and mid-infrared linestrengths of H_2O and CO_2 at 2000 K (from HITRAN2016). (a) H_2O; (b) CO_2

等重金属氟化物组成的复合玻璃光纤;其外径为

192 μm,纤芯芯径为 100 μm,使用标准截断法测得的损耗为 0.13 dB/m@2.5 μm。由于 ZBLAN 光纤损耗较高,为了保证较高的信号强度,在流场探测的实际应用中的光纤长度为 0.5～1.0 m,故实验中截取 0.5 m 光纤作为传输介质。

该系统采用 Nanoplus GmbH 公司生产的中红外分布式反馈(DFB)激光器作为光源,其中心波长在 2.5 μm 附近,稳定输出功率约为 10 mW,同时利用激光控制箱对 DFB 激光器进行温度和电流调控,从而实现对目标波长的覆盖扫描。光源出射激光经过透镜(L1、L2)准直、聚焦后耦合进入 ZBLAN 光纤或者反谐振空芯光纤,从光纤出射的激光信号经过准直镜 L3 准直之后,使用热释电阵列相机(Ophir Pyrocam ⅢHR)进行图像采集,由光电探测器(Thorlabs,PDA10D2)实现光电转换,最后利用上位机的数据采集卡(National Instruments,PCIE 6361)采集波形信号。

AR-HCF: anti-resonant hollow core fiber; DAQ: data acquisition card; L: lens; CCD: charge coupled device; PD: photo-detector
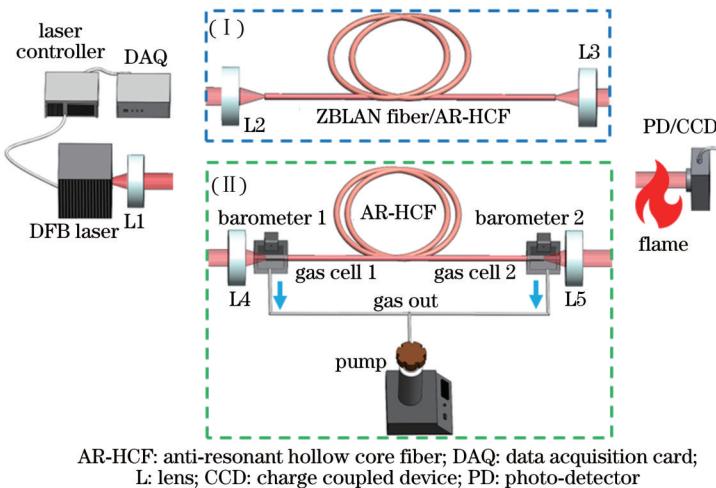
图 7 TDLAS 系统示意图
Fig. 7 TDLAS system diagram

4 基于光纤的 TDLAS 性能表征

4.1 经过燃烧区域的空间激光光束质量

在 TDLAS 系统中,光纤输出光斑的尺寸、能量是否集中,决定了空间激光光束经过燃烧区域后的信号采集难易程度、信号强弱以及探测器能否放置在安全距离。为了检测 ZBLAN 光纤与反谐振空芯光纤出射光斑效果,将两种光纤出射光束分别经过透镜 L3、L5 准直,并将热释电阵列相机(Ophir Pyrocam ⅢHR)分别放置在距离透镜 10、20、30、40、50 cm 的位置。测量结果如表 1 所示,其中 ZBLAN 光纤出射光斑直径为 D_1,反谐振空芯光纤出射光斑直径为 D_2。当探测距离为 50 cm 时,ZBLAN 光纤的发散角约为 0.016 rad,出射光斑的直径为 9.3 mm,反谐振空芯光纤的发散角约为 0.004 rad,光斑直径为 2.5 mm。

如图 8 第二行光斑所示,使用 ZBLAN 光纤作为传

表 1 ZBLAN 光纤和反谐振空芯光纤出射光束准直后不同距离处光斑直径的测量结果

Table 1 Measurement results of spot diameter at different distances after collimating the output beam of ZBLAN fiber and AR-HCF

L /cm	D_1 /mm	D_2 /mm
10	1.4	0.7
20	2.6	1.0
30	4.6	1.4
40	7.2	1.9
50	9.3	2.5

输介质时光信号较弱、光斑弥散范围大,精细化的空间光路调整能够改善这一缺陷。但是 ZBLAN 光纤作为多模光纤,在能量传输过程中出现高阶模式,导致其出射光斑形状不规则、能量分布不均匀、能量损耗高的弊端无法通过简单的空间光路耦合来改变。反谐振空芯

光纤的空间光耦合效率高、传输损耗低,这是因为其独特的导光机理使高阶模式成分得以高效滤除,从而在纤芯中实现长距离准单模传输。如图 8 第一行所示,反谐振空芯光纤出射光斑为圆形、范围小且能量集中,极大地提高了系统的信号强度,同时降低了信号收集的难度。
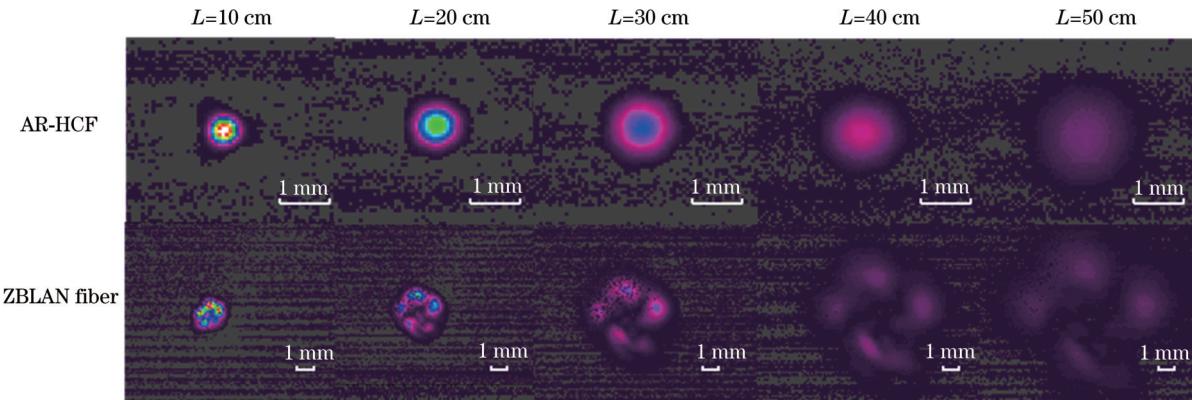

图 8 准直后不同距离处的出射光斑

Fig. 8 Spots at different distances after collimation

4.2 光谱吸收信号的信噪比

信噪比(R_{SNR})是指系统中信号和噪声的比值,是衡量系统输出信号质量的重要参数之一。通常情况下,信噪比越大,输出信号质量越高。

$$R_{\mathrm{SNR}} = 20\lg(V_{\mathrm{s}}/V_{\mathrm{n}}), \quad (7)$$

式中:V_{s} 为信号扣除基线、线型拟合后的峰值;V_{n} 为背景噪声的平均值。实验中首先使用长度为 0.5 m 的 ZBLAN 光纤作为传输介质,将光电探测器放在与准直镜 L3 相隔 10 cm 的位置,并且在 L3 与探测器之间使用打火机(燃料为丁烷)点火,以此获得一个强吸收谱线便于测量演示。火焰燃烧时产生高温水汽,激光从燃烧流场中通过,利用光电探测器收集此时的激光信号,并完成光电转换,得到的吸收光谱信号如图 9 所示。

从图 9(a)可以看到,ZBLAN 光纤作为传输介质时吸收光谱线是一条充满干涉条纹的曲线,主要原因是 ZBLAN 光纤在传输激光过程中不仅有基模,还产生了若干个高阶模式,模式之间发生干涉,产生幅值较大的干涉条纹。从图 9(b)可以看到,基于反谐振空芯光纤的吸收谱线较为平滑,这是因为反谐振空芯光纤在传输激光时,光纤中只存在基模。由信噪比公式计算得出,基于 ZBLAN 光纤的系统信噪比为 17 dB,基于反谐振空芯光纤的系统信噪比为 31 dB。显而易见,相较于 ZBLAN 光纤,反谐振空芯光纤利用单模传输的优势,有效地消除了模间干涉,将系统的信噪比提升了 14 dB。
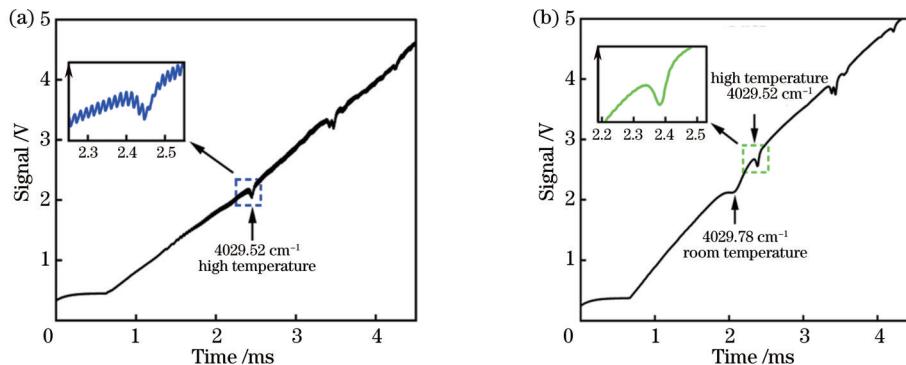
图 9 不同传输光纤的高温水汽吸收信号。(a) ZBLAN 光纤作为传输介质时高温水汽吸收信号,其中 4029.52 cm^{-1} 为高温水汽吸收线;(b)反谐振空芯光纤作为传输介质时高温水汽吸收信号,其中 4029.78 cm^{-1} 和 4029.52 cm^{-1} 分别为室温水汽吸收线和高温水汽吸收线

Fig. 9 High temperature water vapor absorption signal of different transmission fibers. (a) High-temperature water vapor absorption signal when ZBLAN optical fiber is used as the transmission medium, and 4029.52 cm^{-1} is the high-temperature water vapor absorption line; (b) high temperature water vapor absorption signal when AR-HCF is used as the transmission medium, and 4029.78 cm^{-1} and 4029.52 cm^{-1} are the water vapor absorption lines at room temperature and high temperature, respectively

4.3 反谐振空芯光纤中痕量水汽对 TDLAS 测量的影响

如图 9(b)所示,使用空气填充的反谐振空芯光纤作为传输介质,有效地提高了系统信噪比,但在 4029.52 cm^{-1} 目标高温水汽吸收线附近出现了常温水汽吸收线 4029.78 cm^{-1}(来自 HITRAN2016 数据库)。反谐振空芯光纤中痕量水汽来源大致分为两种:一部分来源于空芯光纤在拉制过程中玻璃材料的释放;另一部分为从光纤微结构的两端扩散到纤芯空气中的水汽[28]。为了进一步研究反谐振空芯光纤残留的痕量水汽对于 4029.52 cm^{-1} 谱线测量的影响,在环境干燥的超净室中进行演示实验,并且在 3.3 节搭建的系统上增加了对空芯光纤进行抽真空的装置,如图 7(Ⅱ)所示,由于系统的光源、光源的控制系统和探测器并未改变,因此未在(Ⅱ)中重复展示。DFB 激光器准直出射的激光通过透镜 L4 聚焦后耦合进入光纤,光纤的两端放置在密闭的气室中,气室与真空分子泵(PFEIFFER, D-35614 Asslar TC110)连接并且装有真空气压计(爱德机电科技有限公司,VR-208C-510EF-C1-Maxs-2),光纤尾端出射激光通过准直镜 L5 准直之后进入燃烧流场和探测器。

反谐振空芯光纤中残留的痕量水汽使得激光在空芯光纤中传输时部分能量被光纤中的水汽吸收,从而产生 4029.78 cm^{-1} 常温水汽吸收线。常温水汽吸收线的存在提高了目标信号 4029.52 cm^{-1} 的基线拟合难度,增加了由数据处理引入的误差[29]。为了降低 4029.78 cm^{-1} 吸收线的干扰,对空芯光纤进行长时间(＞1 h)抽真空处理[30],以使空芯光纤内部保持干燥。如图 10 所示,经过抽真空处理后的反谐振空芯光纤吸收线 4029.78 cm^{-1} 的峰值减小且线宽变窄,与 4029.52 cm^{-1} 的吸收谱线不再重叠,从而提高了基线拟合的准确度和系统的检测精度[31]。
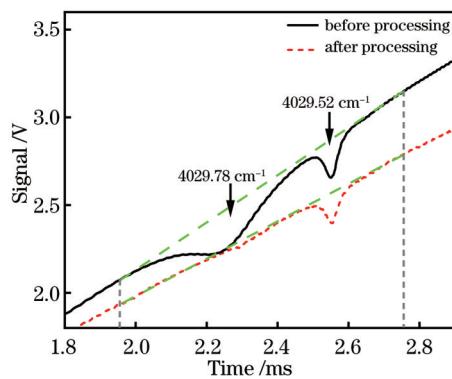

图 10 反谐振空芯光纤抽真空前后的基线拟合对比

Fig. 10 Comparison of baseline fitting before and after vacuum pumping of AR-HCF

5 结 论

搭建了基于光纤的 TDLAS 系统,对比了使用自研反谐振空芯光纤和商用 ZBLAN 光纤的 TDLAS 系统对于高温水汽吸收测量的性能。实验结果显示,基于反谐振空芯光纤的 TDLAS 系统的传输损耗低并且实现 2.5 μm 的单模传输,将能量集中在直径为 2.5 mm 的光斑,该光斑直径远小于 ZBLAN 光纤输出光斑的直径,有利于增强信号强度、方便信号收集。同时,反谐振空芯光纤单模传输从根本上消除了多模干涉对于 TDLAS 测量精度的影响,相较于使用 ZBLAN 光纤的系统,其测量信噪比提高了 14 dB。进一步分析了反谐振空芯光纤残留的痕量水汽对于 4029.52 cm^{-1} 谱线测量的影响,实验中通过抽真空装置将空气填充的反谐振空芯光纤真空化,可以降低室温水汽吸收线 4029.78 cm^{-1} 的干扰,进一步提升系统的测量精度。综上所述,基于反谐振空芯光纤的 TDLAS 系统具有传输损耗低、传输距离长、输出光束质量高、信噪比高等优点。所提方法为发展中红外波段的流场探测提供了新思路。

参 考 文 献

[1] Griffiths A D, Houwing A F P. Diode laser absorption spectroscopy of water vapor in a scramjet combustor[J]. Applied Optics, 2005, 44(31): 6653-6659.

[2] Schultz I A, Goldenstein C S, Jeffries J B, et al. Diode laser absorption sensor for combustion progress in a model scramjet [J]. Journal of Propulsion and Power, 2014, 30(3): 550-557.

[3] Fang S H, Wang Z Z, Lin X, et al. Characterizing combustion of a hybrid rocket using laser absorption spectroscopy[J]. Experimental Thermal and Fluid Science, 2021, 127: 110411.

[4] Brown M, Barone D, Barhorst T, et al. TDLAS-based measurements of temperature, pressure, and velocity in the isolator of an axisymmetric scramjet[C]//46th AIAA/ASME/SAE/ASEE Joint Propulsion Conference & Exhibit, July 25-28, 2010, Nashville, TN. Virigina: AIAA Press, 2010: 6989.

[5] Rieker G B, Li H, Liu X, et al. Rapid measurements of temperature and H$_2$O concentration in IC engines with a spark plug-mounted diode laser sensor[J]. Proceedings of the Combustion Institute, 2007, 31(2): 3041-3049.

[6] 李飞, 余西龙, 陈立红, 等. TDLAS 测量甲烷/空气预混平面火焰温度和 H$_2$O 浓度[J]. 实验流体力学, 2009, 23(2): 40-44.
Li F, Yu X L, Chen L H, et al. Temperature and water vapour concentration measurements of CH$_4$/Air premixed flat flame based on TDLAS[J]. Journal of Experiments in Fluid Mechanics, 2009, 23(2): 40-44.

[7] Schultz I A, Goldenstein C S, Jeffries J B, et al. Spatially-resolved TDLAS measurements of temperature, H$_2$O column density, and velocity in a direct-connect scramjet combustor [C]//52nd Aerospace Sciences Meeting, January 13-17, 2014, National Harbor, Maryland. Virigina: AIAA Press, 2014: 1241.

[8] Farooq A, Jeffries J B, Hanson R K. In situ combustion measurements of H$_2$O and temperature near 2.5 μm using tunable diode laser absorption[J]. Measurement Science and Technology, 2008, 19(7): 075604.

[9] Ma L H, Ning H B, Wu J J, et al. In situ flame temperature measurements using a mid-infrared two-line H$_2$O laser-absorption thermometry[J]. Combustion Science and Technology, 2018, 190(3): 393-408.

[10] Goldenstein C S, Spearrin R M, Jeffries J B, et al. Infrared laser absorption sensors for multiple performance parameters in a detonation combustor[J]. Proceedings of the Combustion Institute, 2015, 35(3): 3739-3747.

[11] Cassady S J, Peng W Y, Strand C L, et al. Time-resolved, single-ended laser absorption thermometry and H_2O, CO_2, and CO speciation in a H_2/C_2H_4-fueled rotating detonation engine[J]. Proceedings of the Combustion Institute, 2021, 38(1): 1719-1727.

[12] Clees S, Cha D H, Biswas P, et al. A laser-absorption sensor for *in situ* detection of biofuel blend vapor in engine intakes[EB/OL]. [2022-11-08]. https://www. sciencedirect. com/science/article/pii/S1540748922001456?via%3Dihub.

[13] Belardi W. Design and properties of hollow antiresonant fibers for the visible and near infrared spectral range[J]. Journal of Lightwave Technology, 2015, 33(21): 4497-4503.

[14] Harrington J A. A review of IR transmitting, hollow waveguides [J]. Fiber and Integrated Optics, 2000, 19(3): 211-227.

[15] Kriesel J M, Gat N, Bernacki B E, et al. Hollow core fiber optics for mid-wave and long-wave infrared spectroscopy[J]. Proceedings of SPIE, 2011, 8018: 80180V.

[16] Peng W Y, Goldenstein C S, Spearrin R M, et al. Single-ended mid-infrared laser-absorption sensor for simultaneous *in situ* measurements of H_2O, CO_2, CO, and temperature in combustion flows[J]. Applied Optics, 2016, 55(33): 9347-9359.

[17] Zhu X Y, Wu D K, Wang Y Z, et al. Delivery of CW laser power up to 300 Watts at 1080 nm by an uncooled low-loss anti-resonant hollow-core fiber[J]. Optics Express, 2021, 29(2): 1492-1501.

[18] Zhu X Y, Yu F, Wu D K, et al. Low-threshold continuous operation of fiber gas Raman laser based on large-core anti-resonant hollow-core fiber[J]. Chinese Optics Letters, 2022, 20 (7): 071401.

[19] Cui Y L, Huang W, Zhou Z Y, et al. Highly efficient and stable coupling of kilowatt-level continuous wave laser into hollow-core fibers[J]. Chinese Optics Letters, 2022, 20(4): 040602.

[20] He C, Zhou C, Zhou Q, et al. Simultaneous measurement of strain and temperature using Fabry-Pérot interferometry and antiresonant mechanism in a hollow-core fiber[J]. Chinese Optics Letters, 2021, 19(4): 041201.

[21] Kolyadin A N, Kosolapov A F, Pryamikov A D, et al. Light transmission in negative curvature hollow core fiber in extremely high material loss region[J]. Optics Express, 2013, 21(8): 9514-9519.

[22] Wu D K, Yu F, Liao M S. Understanding the material loss of anti-resonant hollow-core fibers[J]. Optics Express, 2020, 28 (8): 11840-11851.

[23] Yu F, Song P, Wu D K, et al. Attenuation limit of silica-based hollow-core fiber at mid-IR wavelengths[J]. APL Photonics, 2019, 4(8): 080803.

[24] Fu Q, Wu Y D, Davidson I A, et al. Hundred-meter-scale, kilowatt peak-power, near-diffraction-limited, mid-infrared pulse delivery via the low-loss hollow-core fiber[J]. Optics Letters, 2022, 47(20): 5301-5304.

[25] Jaworski P, Kozioł P, Krzempek K, et al. Antiresonant hollow-core fiber-based dual gas sensor for detection of methane and carbon dioxide in the near- and mid-infrared regions[J]. Sensors, 2020, 20(14): 3813.

[26] Duguay M A, Kokubun Y, Koch T L, et al. Antiresonant reflecting optical waveguides in SiO_2-Si multilayer structures[J]. Applied Physics Letters, 1986, 49(1): 13-15.

[27] Goldenstein C S, Hanson R K. Diode-laser measurements of linestrength and temperature-dependent lineshape parameters for H_2O transitions near $1.4\mu m$ using Voigt, Rautian, Galatry, and speed-dependent Voigt profiles[J]. Journal of Quantitative Spectroscopy and Radiative Transfer, 2015, 152: 127-139.

[28] Kobelke J, Bierlich J, Schuster K, et al. OH diffusion effects at preparation of antiresonant hollow core fibers[J]. Proceedings of SPIE, 2019, 11029: 1102904.

[29] 朱晓睿, 卢伟业, 饶雨舟, 等. TDLAS直接吸收法测量CO_2的基线选择方法[J]. 中国光学, 2017, 10(4): 455-461.
Zhu X R, Lu W Y, Rao Y Z, et al. Selection of baseline method in TDLAS direct absorption CO_2 measurement[J]. Chinese Optics, 2017, 10(4): 455-461.

[30] Li Y, Yang X M, Hao X Y, et al. Study of gas dynamics in hollow-core photonic crystal fibers[J]. Optik, 2021, 246: 167797.

[31] Zhang T Y, Kang J W, Meng D Z, et al. Mathematical methods and algorithms for improving near-infrared tunable diode-laser absorption spectroscopy[J]. Sensors, 2018, 18(12): 4295.

Design and Experimental Study of Mid-Infrared TDLAS System Based on Anti-Resonant Hollow Core Fiber

Sun Yali[1,2], Zhu Xinyue[1], Wu Dakun[1,3], Wu Cheng[1,4], Yu Fei[1,3*], Li Renjie[5,6], Lin Xin[5**], Zhao Wenkai[7]

[1]*Laboratory of Materials for High Power Laser Optical Components, Shanghai Institute of Optics and Fine Mechanics, Chinese Academy of Sciences, Shanghai* 201800, *China*;

[2]*Center of Materials Science and Optoelectronics Engineering, University of Chinese Academy of Sciences, Beijing* 100049, *China*;

[3]*School of Physics and Optoelectronic Engineering, Hangzhou Institute for Advanced Study, University of Chinese Academy of Sciences, Hangzhou* 310024, *Zhejiang, China*;

[4]*School of Physical Sciences, University of Science and Technology of China, Hefei* 230026, *Anhui, China*;

[5]*State Key Laboratory of High-Temperature Gas Dynamics, Institute of Mechanics, Chinese Academy of Sciences, Beijing* 100190, *China*;

[6]*School of Engineering Science, University of Chinese Academy of Sciences, Beijing* 100049, *China*;

[7]*Research Center of Infrared Optical Materials, Shanghai Institute of Optics and Fine Mechanics, Chinese Academy of Sciences, Shanghai* 201800, *China*

Abstract

Objective   Tunable diode laser absorption spectroscopy (TDLAS) plays a key role in non-contact gas measurement, particularly under harsh environmental conditions, such as at high-temperature, and high-pressure situations. The emission of a tunable diode laser in a typical TDLAS system usually propagates in the free space and reaches the measurement zone. Such configuration inevitably suffers the natural diffraction of laser beams, which leads to a dramatic decrease in signal-to-noise ratio for remote measurement. In this case, the application of optical fibers provides a flexible way of delivering laser beams for TDLAS measurement, indicating excellent adaptability. However, under the mid-infrared length of no less than 2 μm, phonon absorption of fused silica will increase the material loss of silica glass optical fibers and reduces their long-distance transmission ability. Benefiting from the low material absorption, fluoride glass fibers based on ZBLAN and chalcogenide glass fibers based on As_2S_3 have become the main optical fibers operating at mid-infrared wavelengths. Unfortunately, such soft glass fibers have disadvantages including poor thermal stability, unstable chemical properties, and difficult preparation. Additionally, nearly all commercial fluoride and chalcogenide fibers on shelves are multimode fibers (MMF), which results in modal interference and poor laser beam quality, thereby leading to degraded TDLAS measurement performance. As a kind of hollow waveguide developed early for transmitting mid-infrared to far-infrared wavelengths, Capillary waveguides have been employed instead of soft glass fibers in high-temperature flow field detection due to their advantages of high-power threshold, low nonlinearity, and no-end reflection. However, they usually suffer high leakage losses and bending sensitivity. Anti-resonant hollow core fiber (AR-HCF) is a new type of microstructure hollow core fiber that features low loss, wide transmission bandwidth, and single mode transmission. AR-HCF is a novel transmission medium suitable for low-loss single mode transmission in the mid-infrared wavelength range, which has been successfully applied in high-power laser energy transmission, gas fiber laser technology, and other fields. Currently, the quartz-based AR-HCF exhibits lower transmission loss in the 2–5 μm range compared with commercial multi-mode fluoride fibers, demonstrating its enormous potential in mid-infrared region transmission. Moreover, due to the inherent advantages of quartz materials, mid-infrared quartz-based AR-HCF features excellent mechanical strength, physical and chemical stability, and good environmental adaptability. This paper constructs TDLAS systems based on AR-HCF and ZBLAN fibers respectively to carry out a combustion diagnostic by the high-temperature water vapor absorption at 2.5 μm. Unlike commercial fluoride and chalcogenide optical fibers, the AR-HCF is characterized by low loss and single-mode transmission in a broad spectral window from deep ultraviolet to mid-infrared. The TDLAS system is demonstrated to be capable of avoiding inter-modal interference that degrades measurement accuracy.

Methods   In this paper, the stack-and-draw method is employed to fabricate the AR-HCF operating at mid-infrared wavelengths. Firstly, some thin-wall capillaries are drawn from a silica glass tube. Then, the capillaries are stacked into a jacket tube to form a pre-designed structure. Next, the stack is drawn into preforms and then fiber, and a cut-back method is adopted to measure the transmission loss of the fiber. The transmission characteristics of fiber are also investigated numerically by COMSOL and the ability of low loss and single mode transmission in the AR-HCF is confirmed. Two

TDLAS systems are built based on the homemade AR-HCFs and ZBLAN fibers respectively. The beam and spectrum of the system are collected through a pyroelectric array camera and photodetector. Analysis of the beam quality and signal-to-noise ratio for both systems exhibits the advantages of the AR-HCF-based TDLAS system. Additionally, the accuracy of the system is improved by evacuating the water vapor inside the AR-HCF.

Results and Discussions   The AR-HCF transmission band prepared in this paper is between 2.4−2.5 μm, and the loss at 2.5 μm is 0.06 dB/m (Fig. 3), which is lower than commercial fluoride glass fibers. Furthermore, COMSOL is adopted to build the AR-HCF mode. The simulation results show that the strong coupling between the second-order mode in the core and the modes in cladding holes results in energy leakage and high loss, thus enhancing the single-mode performance of the fiber (Fig. 4). With these advantages of AR-HCF, TDLAS system is preferred to be employed rather than free space. This paper leverages the homemade AR-HCF in the TDLAS system successfully to realize a signal-to-noise ratio of 31 dB (Fig. 9), which can output a collimated near-diffraction-limited beam with a measured diameter of 2.5 mm (Fig. 8 and Table 1) and divergence angle of 0.004 rad. The influence of residual water vapor in the hollow core of AR-HCF on the measurement of 4029.52 cm^{-1} absorption line is studied, and the accuracy of the system is further improved by vacuuming the AR-HCF (Fig. 10).

Conclusions   This paper presents an AR-HCF-based TDLAS system and compares the performance of self-developed AR-HCF and commercial ZBLAN fiber in the high-temperature water vapor absorption measurement by TDLAS. Simulation and experimental results prove that the AR-HCF can achieve long-distance, low-loss, and single-mode transmission at 2.5 μm. The TDLAS system based on AR-HCF fundamentally eliminates multi-mode interference and has the advantages of the small beam diameter, small divergence angle, and high signal-to-noise ratio. The impact of residual trace water vapor in the AR-HCF on the measurement of the 4029.52 cm^{-1} spectral line is also analyzed and the measurement accuracy of the system is improved by vacuuming it. This paper also designs and experimentally studies the mid-infrared TDLAS system based on AR-HCF. Finally, the system is confirmed to have the advantages of low transmission loss, long transmission distance, high laser beam quality, and high signal-to-noise ratio, which provides a new method for flow field detection in the mid-infrared band.

Key words   fiber; anti-resonant hollow core fiber; laser absorption spectroscopy; multi-mode interference; single mode; combustion diagnosis